International Journal of Nanomedicine

Dovepress
Taylor & Francis Group

Open Access Full Text Article

ORIGINAL RESEARCH

A pH/H_2O_2 Dual-Responsive Cobalt–Manganese-Based Nano-Delivery System for Chemo/Chemodynamic Therapy in Triple-Negative Breast Cancer

Guanghui Mei[1], Fei Lin[1,2], Liying Huang[1], Min Lin[3], Xinhua Lin[1], Lingyi Huang[1]

[1]School of Pharmacy, Fujian Medical University, Fuzhou, 350122, People's Republic of China; [2]College of Chemistry, Fuzhou University, Fuzhou, 350108, People's Republic of China; [3]School of Innovation, Entrepreneurship, and Creation of Minjiang University, Fuzhou, Fujian, 350108, People's Republic of China

Correspondence: Lingyi Huang; Xinhua Lin, School of Pharmacy, Fujian Medical University, Fuzhou, 350122, People's Republic of China, Email lingyi.huang@fjmu.edu.cn; 13906909638@163.com

Purpose: This study developed a dual-responsive nano-delivery system to overcome elevated glutathione (GSH) and acidic pH in the tumor microenvironment (TME), enhancing chemodynamic therapy (CDT) and chemotherapy against triple-negative breast cancer (TNBC).

Methods: A pH/H_2O_2-responsive nanoplatform named as ZIF-67/MnO_2/DOX/BSA/SDS (ZMDBS), was developed by integrating zeolitic imidazolate framework-67 (ZIF-67) with manganese dioxide (MnO_2), loading doxorubicin (DOX), then introducing bovine serum albumin (BSA) and sodium dodecyl sulfate (SDS). Under TME conditions, it released Co^{2+} and Mn^{2+} ions to promote Fenton-like reactions and reactive oxygen species (ROS) generation. Physicochemical properties, GSH/H_2O_2 responsiveness, ROS production, and pH-triggered DOX release were also evaluated. In vitro (cellular uptake, ROS quantification, apoptosis, and migration tests) and in vivo experiments were conducted, alongside transcriptomic profiling.

Results: Characterization results (particle size, zeta potential, FTIR, TEM, XRD, and XPS) confirmed ZMDBS as a novel cobalt/manganese-based nanocomposite, with the encapsulation rate of 95%. It efficiently depleted GSH, enhanced ROS production, and controlled DOX release under TME conditions. In vitro experiments, ZMDBS showed minimal toxicity to LO2 hepatocytes, whereas induced a two-fold ROS increase, 70.7% apoptosis in 4T1 cells (vs 40.9% for DOX), and a lower IC_{50} (0.35 μg/mL vs 5.00 μg/mL for DOX). In vivo, ZMDBS reduced tumor volume by 60.7% in mice without systemic toxicity (vs 31.1% for DOX). Transcriptomics revealed that ZMDBS-triggered ROS overproduction activated the p53, MAPK, and TNF pathways, culminating in caspase-mediated apoptosis.

Conclusion: ZMDBS, a pH/H_2O_2 dual-responsive cobalt/manganese-based nanoplatform, has remodeled the TME for synergistic CDT and chemotherapy. With high catalytic efficiency and favorable biocompatibility, it offers a promising strategy for safe and effective TNBC treatment.

Keywords: chemodynamic therapy, triple-negative breast cancer, tumor microenvironment, cobalt/manganese-based nano-delivery system, ZIF-67/MnO_2/DOX/BSA/SDS

Introduction

Triple-negative breast cancer (TNBC) is characterized by aggressive invasion, high recurrence, and poor prognosis, which presents a significant challenge in clinical treatment.[1] Due to the lack of specific therapeutic targets, TNBC shows resistance to most targeted therapies and has limited available treatment options, with chemotherapy remaining the primary approach.[2] Currently, the chemotherapeutic drugs used for TNBC in clinical practice mainly include doxorubicin (DOX),[3] paclitaxel (PTX),[4,5] and 5-fluorouracil (5-FU),[6] etc. Although these traditional chemotherapy drugs effectively eliminate tumor cells, they still have drawbacks, including instability in systemic circulation,[7] non-specific distribution

Received: 18 July 2025
Accepted: 23 October 2025
Published: 5 November 2025

within the human body,[8] and substantial toxic side effects on normal organs and cells.[9] Consequently, there is ongoing research focused on developing innovative treatment strategies to alleviate the toxic effects of chemotherapy drugs.

As a novel cancer treatment based on Fenton/Fenton-like reactions, chemodynamic therapy (CDT) offers significant advantages such as tumor specificity, independence from external triggers, and a favorable side effect profile.[10,11] In recent years, it has emerged as a revolutionary approach in the field of precise and effective cancer treatment. The fundamental principle of CDT involves the utilization of transition metals, such as ferrum (Fe), manganese (Mn), cobalt (Co), and copper (Cu), as catalysts to facilitate the conversion of excess H_2O_2 into hydroxyl radicals (·OH) in the tumor microenvironment (TME) of TNBC.[12] ·OH, the most harmful reactive oxygen species (ROS), can induce cancer cell death via oxidative damage to lipids, proteins, and DNA.[13] However, the catalytic efficiency of CDT is limited by the high concentrations of GSH (>10 mM) and weakly acidic conditions in the TME.[14,15] Therefore, it is crucial to develop a tailored CDT treatment plan that considers the characteristics of the tumor microenvironment characterized by high levels of H_2O_2 and GSH, along with a weakly acidic condition.

Considerable efforts have been made to modify the TME characteristics. For example, Zhang et al synthesized a nanodrug, DOX@Fe^{3+}-LA (DOX@FL), to deplete excess GSH and H_2O_2 in TME.[16] Xu et al reported that MnO_2 has a TME responsive behavior, demonstrating its ability to react with H^+, H_2O_2, and GSH to deplete excess GSH and H_2O_2 in TME, which could improve the effects of CDT ($MnO_2 + 2GSH + 2H^+ \rightarrow Mn^{2+} + GSSG + 2H_2O$, $MnO_2 + H_2O_2 + 2H^+ \rightarrow Mn^{2+} + 2H_2O + O_2\uparrow$).[17] Although MnO_2 showed promising chemotherapy activity, the instability of MnO_2 in the body's circulation and its uncertain drug-carrying capacity are major obstacles to its effectiveness. Therefore, it is essential to identify nanocarriers that can enhance the stability and therapeutic efficacy of MnO_2.

In this study, we innovatively developed a TME-responsive nano-delivery system named ZIF-67/MnO_2/DOX/BSA/SDS (ZMDBS) for TNBC chemo/chemodynamic combination therapy (Scheme 1). Among them, zeolitic imidazolate framework-67 (ZIF-67) has a large specific surface area and high porosity, allowing easy functionalization. It also exhibits Fenton-like catalytic activity, pH responsiveness, high biocompatibility, and low cytotoxicity. This material remains stable under physiological neutral conditions but can be cleaved under the acidic conditions of the TME, releasing its internal encapsulated chemotherapeutic drugs and exerting their effects, making it a reliable nanocarrier for MnO_2. ZIF-67 generates Co^{2+} as a catalyst for Fenton-like reactions that catalyze the generation of •OH from excess H_2O_2 in the TME to induce apoptosis of tumor cells. Thus, the combination of ZIF-67 and MnO_2 (ZM) not only ensures the stability of MnO_2 in vivo but also enhances the CDT activity.

The chemotherapeutic drug DOX, bovine serum albumin (BSA), and sodium dodecyl sulfate (SDS) were subsequently introduced to form a nano-delivery system, ZMDBS. DOX is a widely used anti-cancer agent that functions by inhibiting topoisomerase II in fast-proliferating tumors. Meanwhile, DOX has been shown to induce NADPH oxidase activation under oxygen-sufficient conditions, leading to the conversion of O_2 to $•O^{2-}$, and subsequent cellular oxidative damage and apoptosis.[18] Moreover, the superoxide dismutase (SOD) in tumor cell can convert $·O_2^-$ into H_2O_2, which provides reactive materials for CDT.[19] BSA has multiple functional sites on its surface which could enable specific binding to ZIF-67, creating a negatively charged system and thereby preventing non-specific interactions with biological components. The protein framework of the system can be degraded and eliminated under weakly acidic conditions in TME, thereby ensuring excellent biocompatibility. SDS, a widely used anionic surfactant, can stabilize nano molecules and improve their biocompatibility. It was incorporated into a nano-delivery system to enhance its stability.

In summary, TNBC remains a formidable clinical challenge due to its aggressive phenotype, lack of targeted receptors (eg, HER2, ER/PR), and inherent resistance to conventional therapies.[1,2] The TME exacerbates these issues through elevated GSH levels, which quench ROS, and acidic conditions that impair drug efficacy and promote metastasis.[14,15] Prior literatures have explored CDT combining metal-based nanomaterials for TME modulation. However, the instability (eg, MnO_2)[16,17] or potential toxicity (eg, Cu)[20] of metal ion limits its application. Dual-stimuli-responsive systems (eg, pH/GSH-responsive) have addressed some gaps.[21] For example, pH/GSH-sensitive metal-organic frameworks (MOFs) by Cao et al integrated CDT with drug release, yet these platforms suffer from aggregation in physiological media and poor accumulation in tumor site.[22] To counteract those issues, the ZMDBS integrates: (1) ZIF-67 provides a stable framework under physiological conditions and targeted to the tumor cells; (2) Co^{2+}/Mn^{2+} converts H_2O_2 to•OH for CDT;

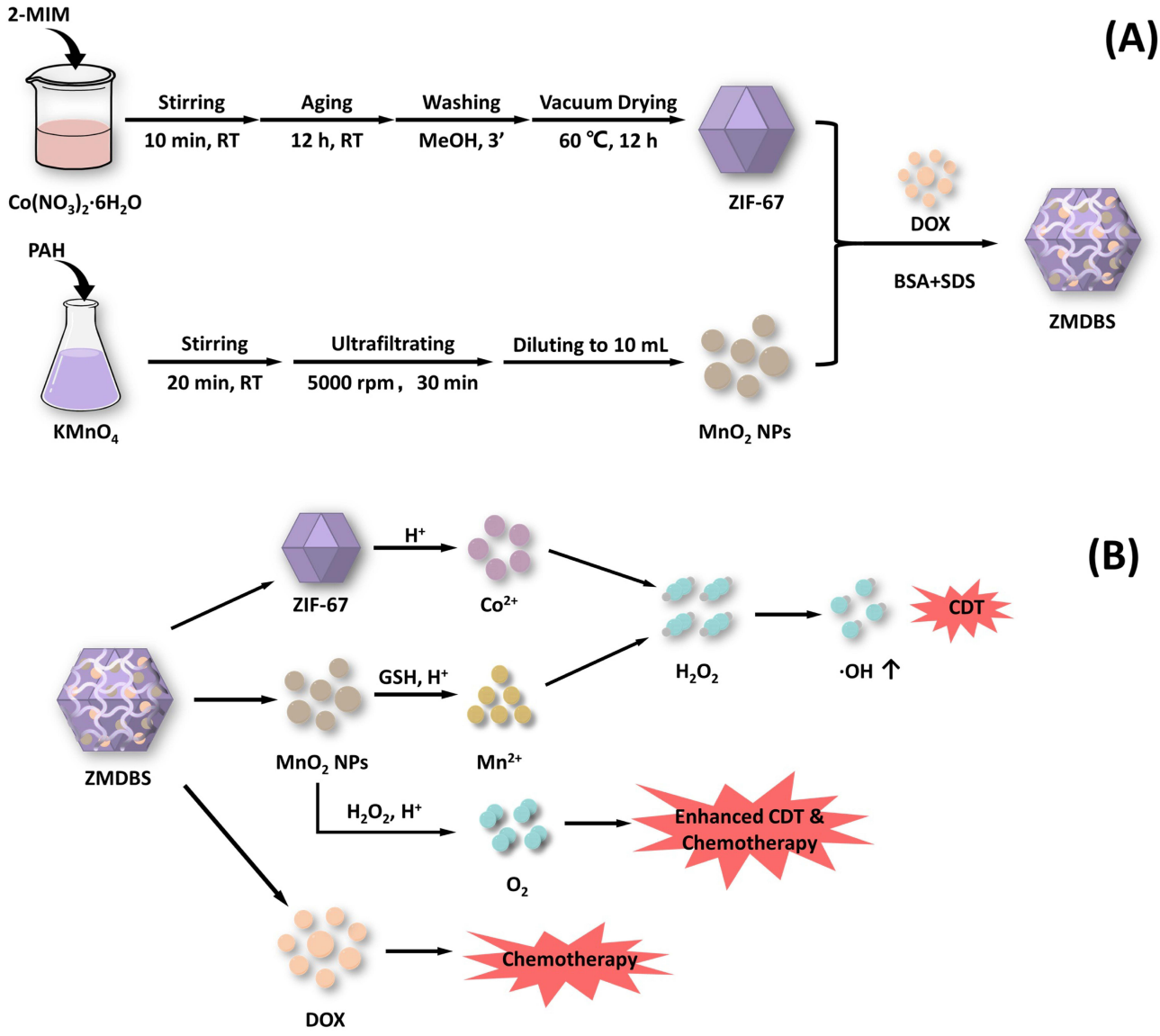

Scheme 1 The synthetic procedure of ZMDBS (**A**) and the schematic diagram of ZMDBS therapeutic mechanism (**B**).

(3) MnO_2-mediates GSH depletion to relieve redox suppression; (4) a pH-responsive system triggers DOX release at the tumor site; (5) BSA and SDS scaffolds that enhance biocompatibility and offer high drug-loading capacity for DOX.

Based on the in vitro and in vivo experimental data, ZMDBS exhibited GSH-responsive, H_2O_2-responsive, and pH-responsive activities, along with potent CDT capabilities that induced ROS production, resulting in the apoptosis and suppression of migration for tumor cells. This nanomaterial takes advantage of TME characteristics for both chemo/chemodynamic therapy, offering a novel approach for treating TNBC with high efficiency and specificity.

Materials and Methods

Materials

Polyallylamine hydrochloride (PAH), cobalt nitrate hexahydrate ($Co(NO_3)_2·6H_2O$), 2-methylimidazole (2-MIM), doxorubicin hydrochloride (DOX), bovine serum albumin (BSA), reduced glutathione (GSH), 5,5'-dithiobis (2-nitrobenzoic acid) (DTNB), methylene blue (MB), 3,3',5,5'-tetramethylbenzidine (TMB), thiazole blue (MTT), dimethyl sulfoxide (DMSO), and amiloride hydrochloride salt hydrate were purchased from Shanghai Aladdin Co., Ltd. (Shanghai, China). Potassium permanganate ($KMnO_4$), sodium dodecyl sulfate (SDS), indocyanine green (ICG), and sodium bicarbonate ($NaHCO_3$) were

https://doi.org/10.2147/IJN.S546671

purchased from Sinopharm Chemical Reagent Co., Ltd. (Shanghai, China). Anhydrous ethanol and 30% hydrogen peroxide (H_2O_2) were purchased from Xilong Scientific Co. Ltd. (Shenzhen, China). Chlorpromazine hydrochloride and genistein were purchased from Shanghai Macklin Co. Ltd. (Shanghai, China). 4',6-Diamidin-2-phenylindole (DAPI), 4% paraformaldehyde, cell viability and toxicity testing kit, cell reactive oxygen species testing kit, and cell apoptosis testing kit were purchased from Shanghai Beyotime Co. Ltd. (Shanghai, China). All the reagents were of analytical grade.

Synthesis of ZIF-67 and MnO_2 Nanoparticles

5 mL methanol solution of 2-methylimidazole (2-MIM, 65.6 mg/mL) was added into 1 mL methanol solution of Co $(NO_3)_2 \cdot 6H_2O$ (29.1 mg/mL) and stirred for 10 min until the solution turned blue purple. After standing for 12 h, the solution was centrifuged at 10000 rpm for 20 min and washed three times with methanol. The obtained precipitate was vacuum dried at 60°C for 12 h to get the nanomaterial ZIF-67.

The MnO_2 nanoparticle preparation was based on the oxidation-reduction reaction of PAH and $KMnO_4$.[23] 5 mL aqueous solution of polyallylamine hydrochloride (PAH, 6.32 mg/mL) was added to 5 mL of an aqueous solution of $KMnO_4$ (3.16 mg/mL) and stirred for 20 min until the solution turned black-brown. It was then centrifuged in a 10 kD ultrafiltration tube to obtain a concentrated solution (5000 rpm for 30 min). The concentrated solution was diluted to 10 mL to obtain the nano MnO_2 solution.

Synthesis of ZMDBS

ZIF-67 was dissolved in ethanol and sonicated for 30 min to ensure a complete dispersion. Then, an appropriate amount of ultrapure water was added to obtain a ZIF-67 solution (1 mg/mL). The above solution (2 mL) was added to 1 mL of the nano MnO_2 solution and stirred for 5 min to obtain a ZIF-67/MnO_2 (ZM) solution. Subsequently, 3 mL BSA and 1 mL SDS were added to the ZM solution and stirred for 1 h. It was then centrifuged to obtain the ZIF-67/MnO_2/BSA/SDS (ZMBS) solution.

3 mL of doxorubicin hydrochloride (DOX, 2 mg/mL) and 3 mL of bovine serum albumin were added to 3 mL of the ZM solution and stirred for 2 min, after which 1 mL SDS was added and stirred for 1 h. The mixed solution was centrifuged and the precipitates were removed to obtain ZIF-67/MnO_2/DOX/BSA/SDS (ZMDBS).

Characterization of ZMDBS

Transmission electron microscopy (TEM, FEI, USA) and scanning electron microscopy (SEM, Hitachi, Japan) were used to observe the morphology of the samples. A nanoparticle size and zeta potential analyzer (Anton Paar, Austria) was used to determine the particle size and potential of the samples. A UV–visible spectrophotometer (Shimadzu, Japan) was used to obtain UV spectra of the samples. A Fourier-transform infrared spectrometer (Thermo Fisher Scientific, USA) was used to obtain the infrared spectra of the samples. X-ray photoelectron spectroscopy (Thermo Fisher Scientific, USA) was used to determine the elemental composition and valence state of the samples, and an X-ray diffractometer (Bruker, Germany) was used to determine the crystal structure of the samples.

GSH Responsiveness

Because of the distinct characteristic UV absorption peak at 250–450 nm of ZM, an equal amount of ZM was used to react with different concentrations of GSH (15.63, 31.25, 62.5, 125, 250, 500, 700, and 1000 μM). By observing the UV absorption curve of ZM at 300–400 nm, we can preliminarily determine whether the nanomaterial reacts with GSH. To further verify the GSH responsiveness of ZM, different concentrations of ZM were reacted with GSH (150 μM). Subsequently, 5,5'-Dithiobis-(2-nitrobenzoic acid) (DTNB, 100 μM) was used as a probe to detect residual GSH levels after the reaction. A UV–visible spectrophotometer was used to record the absorbance of the products at 412 nm.

The Ability of H_2O_2 Responsiveness and ROS Generation

0.2 mL of 3,3',5,5' - tetramethylbenzidine solution (TMB, 10 mM) was added to 1.6 mL of 30% H_2O_2. ZM solutions of different concentrations were added, and the mixture was shaken. The reaction was allowed to proceed for 5 minutes. Finally, a UV–visible spectrophotometer was used to measure the UV–visible absorption spectrum at 350–750 nm.

CDT Catalytic Activity

100 μL GSH (10 mM) was added to different concentrations of the ZM solutions. After thorough mixing, 200 μL $NaHCO_3$ solution (100 mM), 200 μL methylene blue solution (0.20 mM) and 1.3 mL of 30% H_2O_2 solution were sequentially added to the above solution. It was then allowed to stand for 1 h. Subsequently, a UV–visible spectrophotometer was used to detect the UV–visible absorption spectrum at 200–800 nm. In addition, 5,5-dimethyl-1-pyrroline-N-oxide (DMPO) was added to 30% H_2O_2. ZM and ZMDBS were used for this reaction. Finally, an electron paramagnetic resonance (EPR) instrument was used to determine the type of reactive oxygen species generated by the reaction.

pH Responsiveness

The DOX release behavior was studied using a dialysis method. Briefly, ZMDBS solution sealed in dialysis bags (MWCO: 25000 Da) was dialyzed while gently shaking at 37°C against different PBS solutions, including pH 5.5 and pH 7.4. At the present time point, 2 mL of the dialysate was removed for UV–visible measurements at 480 nm. The amount of DOX was determined by comparison with a standard curve ($y = 0.01841x + 0.04084$; $R^2 = 0.99976$).

Cell Culture

4T1 cells (murine triple-negative breast cancer cells) and LO2 cells (human normal hepatocytes) (STR correctly identified) were purchased from Wuhan Servicebio Technology Co., Ltd (Wuhan, China). The cells were cultured in RPMI-1640 medium containing 10% fetal bovine serum, 1% penicillin, and streptomycin, and incubated in an incubator at 37°C with 5% CO_2.

Cellular Uptake Experiment

Cellular uptake of the ZMDBS nano-delivery system was investigated using a confocal laser scanning microscope (CLSM, Leica, Germany) and a flow cytometer (FACS Canto II, BD, USA). The 4T1 cells were treated with the ZMDBS nano-delivery system (including 2.5 μg/mL DOX) for 3, 6, and 9 h. The cells were then observed using CLSM and quantified using FACS. Several 4T1 cells were treated with different concentrations of ZMDBS (1, 2, 3, 4, and 5 μg/mL DOX) and quantified using a flow cytometer (FACS Canto II, BD, USA).

Exploration of Endocytosis Pathway

Endocytosis inhibition experiments were performed to elucidate the internalization pathway of ZMDBS. The 4T1 cells (1×10^5 cells/well) were seeded in 12-well plates. After overnight incubation, the cells were pretreated with 1mL RPMI-1640 medium (control group), 50 μM chlorpromazine hydrochloride (CPZ group), 25 μM amiloride hydrochloride (AMI group), and 200 μM genistein (GEN group) at 37°C for 2 h. The 4°C group was incubated at 4°C for 2 h, respectively. Afterward, the cells were incubated with ZMDBS (including 2.5 μg/mL DOX) for 3 h. Finally, the cells were harvested and analyzed through FACS.

Living and Death Cells Staining

The cytotoxicity of the nano-delivery system was first studied by calcein-AM/PI staining of live/dead cells. The 4T1 cells (4×10^4 cells/well) were seeded in 24-well plates. After overnight incubation, the cells were co-incubated with different nanoparticles (at a concentration of 5 μg/mL according to DOX concentration) in 96-well plates for 24 h. Each group of cells was stained with calcein-AM (green: live cells) and PI (red: dead cells) for 30 min. Finally, cells were observed under an inverted fluorescence microscope (Leica, Germany).

In vitro Cytotoxicity Assay

4T1 (4×10^3/well) and LO2 cells (8×10^3/well) were seeded in 96-well plates. After overnight incubation, the cells were incubated with different concentrations of PBS, free DOX, ZMBS, or ZMDBS for 24 h. Cell viability was evaluated using the MTT assay and determined using the following formula:

$$\text{Cell viability (\%)} = \frac{A_{sample} - A_{Blank}}{A_{control} - A_{Blank}}$$

Hemolysis Test

Fresh blood from healthy mice was collected into anticoagulant tubes. After centrifugation (1500 rpm) at 4°C for 15 min, red blood cells (RBCs) were collected and diluted to 2% (v/v) with PBS. Subsequently, RBCs were incubated with different concentrations of ZMDBS at 37°C for 2 h and then centrifuged (10000 rpm) at 25°C for 15 min to obtain the supernatant. PBS solution and ultrapure water were used as negative and positive controls, respectively. Finally, the absorbance (540 nm) was measured using a microplate reader, and the hemolysis rate was calculated from three parallel experiments using the following formula:

$$\text{Hemolysis rate (\%)} = \frac{A_{sample} - A_{negative}}{A_{positive} - A_{negative}} \times 100\%$$

Detection of Intracellular ROS Generation

Intracellular ROS production was detected using the DCFH-DA Assay Kit. 4T1 cells were inoculated in a 6-well plate and co-incubated with a medium containing DOX, ZMBS, or ZMDBS nanoparticles (at a concentration of 3 μg/mL, depending on DOX concentration) for 24 h. Each group was treated with DCFH-DA probe for 20 min and washed three times with PBS. Finally, ROS production was observed using an inverted fluorescence microscope (Leica, Germany) and quantified using FACS.

Cell Apoptosis Assay

Apoptosis was detected using an Annexin V-FITC/PI Apoptosis Detection Kit. 4T1 cells were seeded in 6-well plates and incubated overnight for complete growth. After removing the medium, the cells were co-cultured with PBS, DOX, ZMBS, or ZMDBS (at a concentration of 2.5 μg/mL depending on DOX concentration) for 24 h. After washing with PBS, cells were stained with annexin V-FITC and propidium iodide (PI) for 15 min. The cells were collected and quantified by FACS.

Transcriptome Analysis

4T1 cells were seeded in a 100 mm cell culture dish at a density of 1×10^6 cells/dish and cultured overnight. Subsequently, cells were co-cultured with equal amounts of PBS and ZMDBS (n = 3) for 24 h. The culture medium was then discarded. Cells were washed twice with PBS and digested with trypsin. After washing twice with PBS, samples were obtained for analysis. The samples were processed using the TRIzol reagent. The obtained RNA was subjected to transcriptome sequencing and bioinformatics analysis.

Mouse Tumor Model

All animal experiments in this study were approved by the Animal Care and Use Committee of the Fujian Medical University (No. IACUC FJMU 2023–0201) in accordance with the Guidelines for Animal Experimentation. Female BALB/c mice (6–8 w, 18–22 g) were purchased from Beijing Huafukang Biotechnology Co. (Beijing, China). Each mouse was subcutaneously injected with 6×10^5 4T1 cells to establish the TNBC mouse model.

In vivo Biodistribution Studies

When the tumor volume of the mice reached approximately 100 mm^3, 10 BALB/c ruffled mice were randomly selected and divided into two groups. One group was injected with ICG-labelled ZMBS via the tail vein, whereas the other group was injected with ICG alone (control group). Fluorescence images of live mice were captured at predetermined time points (3, 6, 12, and 24 h) using the IVIS Spectral Imaging System, and the tumor sites are circled for quantitative analysis. To analyze the fluorescence intensity of the nanomaterials in different mouse tissues, 24 mice were injected with ICG and ICG-labelled ZMBS in the tail vein.

Subsequently, the mice were euthanized and their hearts, livers, spleens, lungs, and kidneys were removed. Fluorescence images were captured at predefined time points (3, 6, 12, and 24 h) and quantitatively analyzed using an IVIS spectral imaging system.

In vivo Anticancer Efficacy Evaluation

Upon reaching a tumor volume of approximately 100 mm^3, mice were randomly divided into four groups. The groups were labelled as saline (control), ZMBS, DOX, and ZMDBS. Each group consisted of five mice. These mice received treatment every other day for a total of three times. The first tail vein administration, which occurred on day 0, was performed at a dosage of 1.0 mg/kg. The physical conditions of the mice were monitored daily. The body weight and tumor volume of each mouse were recorded every two days. The tumor volume of mice was calculated according to the following formula (L for length and W for width):

$$V\left(mm^3\right) = \frac{LW^2}{2}$$

After the 12th day, blood was collected for the tests of liver and kidney function indexes. When the mice were executed, their hearts, livers, spleens, lungs, kidneys, and tumors were taken and immersed in 4% paraformaldehyde for 24 h subsequently. Tumor tissues were stained with H&E, TUNEL, and Ki67. The major organs (heart, liver, spleen, lungs, and kidneys) were also subjected to H&E staining.

Statistical Analysis

Statistical analysis was performed using one-way analysis of variance (ANOVA) and t-tests to determine statistical differences between the groups. Results are expressed as mean ± standard deviation (mean ± SD). Each group contained at least 3 parallel samples. $p < 0.05$ considered statistically significant; ns, not statistically significant; * $p < 0.05$, ** $p < 0.01$, *** $p < 0.001$.

Results and Discussion

Characterization of ZIF-67 and MnO_2

Although ZIF-67 has been employed extensively as a metal-organic framework material in a multitude of fields, including electrochemistry,[24] electrocatalysis,[25] photocatalysis,[26] and adsorption,[27] there is no standardized definition or synthesis method for ZIF-67.[28] This is attributed to the fact that ZIF-67 synthesized with different reactant ratios exhibits varying morphological characteristics and functional properties. By adjusting the molar ratios of reactants (n/n) and comparing key indicators, such as the particle size and morphology of the resulting ZIF-67 at each ratio, we were able to identify the most suitable ZIF-67 for the nano-delivery system designed in this study. As shown in Figure 1A, when the molar ratio of 2-methylimidazole to $Co(NO_3)_2{\cdot}6H_2O$ was 2:1, the resulting ZIF-67 exhibited a regular hexagonal shape with a particle size of approximately 2–5 μm. As the molar ratio increased, the particle size of ZIF-67 continuously decreased. The particle size of ZIF-67 at different ratios was examined using a nanoparticle size and zeta potential analyzer (Anton Paar, Austria) (Figure 1B). The particle size was less than 500 nm when the molar ratio reached 12:1 and above, then gradually stabilized between 200 and 300 nm, with the smallest average particle size of 228.9 ± 15.45 nm at 40:1. Thus, a molar ratio of 40:1 was selected as the most suitable for the synthesizing of ZIF-67. Figure 1C shows that ZIF-67 with a molar ratio of 40:1 exhibited a dodecahedral shape. Additionally, the XRD pattern of the prepared ZIF-67, depicted in Supplementary Materials Figure S1, was consistent with previous reports,[29] indicating the excellent crystal structure of ZIF-67.

After conducting experiments with different reactant feed ratios (m/m), the optimal feed ratio for the synthesis of the MnO_2 nanoparticles was determined. This was achieved by comparing the UV–visible absorption spectra and particle size maps of the products obtained at each feed ratio. Figure 1D shows the disappearance of the characteristic peaks of $KMnO_4$ (315, 525, and 545 nm) upon the addition of PAH, along with the emergence of new broad peaks at 300–400 nm, indicating the formation of MnO_2 nanoparticles. The particle size map (Figure 1E) shows a small broad peak at approximately 10 nm when the ration of $KMnO_4$ to PAH was 1:0.5 and 1:1, indicating incomplete encapsulation of MnO_2 by the polyelectrolyte layer (Figure 1F). As the PAH concentration increased, MnO_2 progressively became encapsulated. When the ratio of $KMnO_4$: PAH was 1:2, the small broad

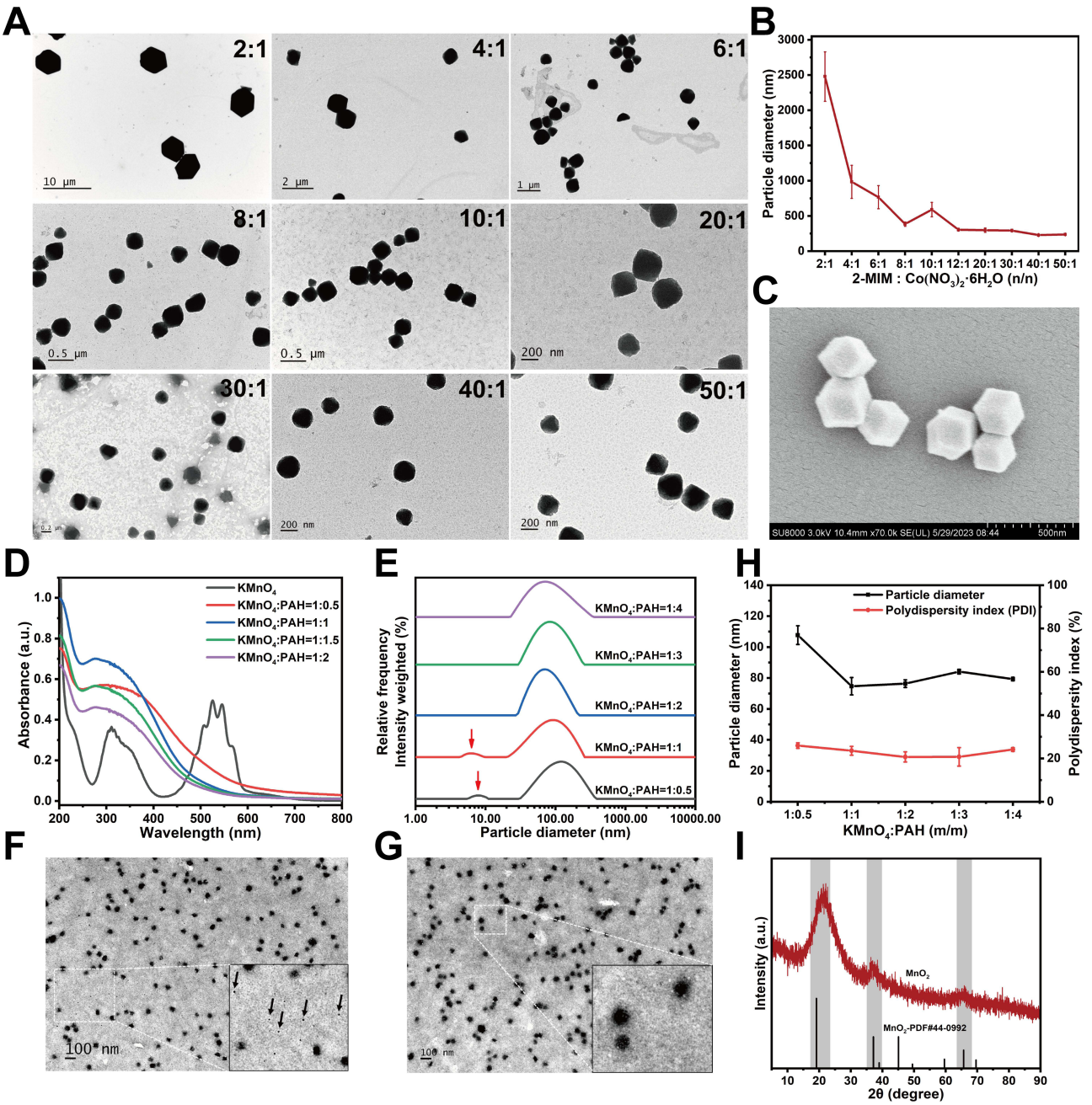

Figure 1 (**A**) TEM images of ZIF-67 obtained from different feeding ratios; (**B**) Particle size of ZIF-67 obtained from different feeding ratios (mean ± SD, n = 3); (**C**) SEM image of ZIF-67 at a feeding ratio of 40:1; (**D**) UV–visible spectra of the products after the reaction between different ratios of $KMnO_4$ and PAH; (**E**) Particle size distribution of the products after the reaction between different ratios of $KMnO_4$ and PAH; (**F**) TEM image of MnO_2 nanoparticles not fully encapsulated by polyelectrolyte; (**G**) TEM image of MnO_2 nanoparticles fully encapsulated by polyelectrolyte; (**H**) Particle size distribution of MnO_2 nanoparticles not completely encapsulated by polyelectrolyte compared with PDI (mean ± SD, n = 3); (**I**) XRD image of MnO_2 nanoparticles.

peak disappeared, suggesting complete wrapping of MnO_2 by the polyelectrolyte and formation of an excess PAH protective layer around the nanoparticles, stabilizing MnO_2 in a state resistant to polymerization and precipitation (Figure 1G).[23] After comparing the particle size and PDI at different feeding ratios (Figure 1H), and considering the factors such as reagent wastage due to excess PAH, it was determined that a ratio ($KMnO_4$: PAH) of 1:2 was the optimal feeding ratio for the synthesis of MnO_2. As illustrated in Figure 1I, the XRD pattern of the synthesized MnO_2 nanoparticles was compared with that of standard MnO_2 (PDF#44-0992); and the two diffraction peaks were found to be highly overlapped, confirming the form of MnO_2 as λ-MnO_2.

Characterization of ZMDBS

The nano-delivery system ZIF-67/MnO_2/DOX/BSA/SDS (ZMDBS) was synthesized via a one-pot method using ZIF-67 as a carrier loaded with MnO_2 and DOX, with the addition of BSA to impart a negative potential to the nanomaterial, and SDS served as a stabilizing agent. The TEM images of ZMDBS (Figure 2A) and ZMBS (Figure S2A) indicated that ZMDBS was spherical and well dispersed compared with ZMBS. The Zeta potentials of MnO_2, ZIF-67, ZIF-67/MnO_2 (ZM), ZIF-67/MnO_2/BSA/SDS (ZMBS), and ZIF-67/MnO_2/DOX/BSA/SDS (ZMDBS) are shown in Figure 2B, where the nanomaterial shifted from positive to negative after the addition of BSA and SDS. The potential of ZMDBS was

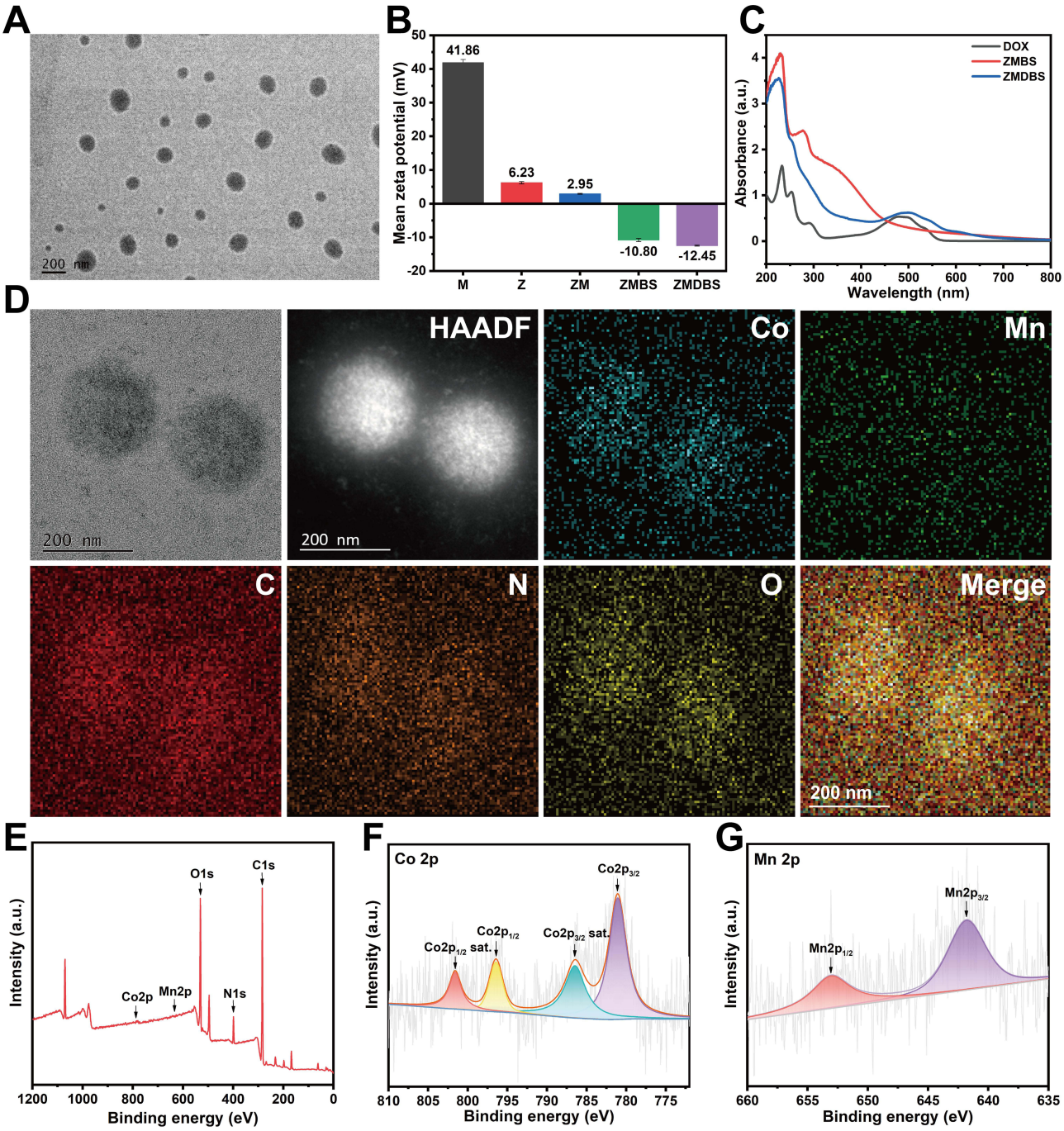

Figure 2 (**A**) TEM map of ZMDBS; (**B**) Zeta potential maps of MnO_2, ZIF-67, ZM, ZMBS and ZMDBS (mean ± SD, n = 3); (**C**) UV–visibl absorption spectra of DOX, ZMBS and ZMDBS; (**D**) EDX elemental maps of ZMDBS; (**E**) XPS survey maps of ZMDBS; (**F**) Cobalt elemental Co2p spectra of ZMDBS; (**G**) Mn2p spectra of ZMDBS.

https://doi.org/10.2147/IJN.S546671

−12.45 ± 0.14 mV. The hydrated particle size of ZMDBS was 270.44 nm (Figure S2B). Fourier-transform infrared (FTIR) spectroscopy (Figure S2C) showed the characteristic absorption peaks of DOX at 550–800 cm^{-1} appeared in the fingerprint region of ZMDBS, and the characteristic absorption peaks at 1300–1500 cm^{-1} were enhanced, indicating that DOX was successfully loaded into ZMDBS. XRD analysis of ZIF-67, MnO_2, ZM, and ZMDBS (Figure S2D) confirmed the amorphization of synthesized ZMDBS. As illustrated in the UV–visible spectrogram (Figure 2C), the characteristic absorption peak of DOX was observed at approximately 480 nm in ZMDBS compared to that in ZMBS. This observation, in conjunction with the FTIR graph, provided further evidence for the successful encapsulation of DOX in ZMDBS. Subsequently, the encapsulation rate and drug loading of DOX in ZMDBS were calculated from the UV characteristic absorption peaks of DOX (Figure S2E) and the standard curve (Figure S2F), which were 95.03 ± 2.27% and 11.40 ± 0.28%, respectively.

The EDX elemental map (Figure 2D) demonstrated that Co, Mn, C, N, and O were uniformly distributed within the ZMDBS nanoparticles. Subsequently, an X-ray photoelectron spectrometer (Thermo Fisher, USA) was employed to determine the elemental composition, chemical valence states, and percentage of each component of ZMDBS. As shown in Figure 2E, ZMDBS was mainly consisted of carbon (C), oxygen (O), nitrogen (N), manganese (Mn) and cobalt (Co) elements. Among them, the binding energy of C1s was 284.78 eV, which accounted for 71.8% of the total composition of ZMDBS; the binding energy of N1s was 399.82 eV, which accounted for 6.62% of the total composition of ZMDBS; and the binding energy of O1s was 531.81 eV, which accounted for 20.94% of the total composition of ZMDBS. The high-resolution spectrum of Co2p (Figure 2F) revealed that the Co2p peak exhibited a markedly split spin-orbit component (Δ_{metal} = 14.99 eV) consisting of two principal peaks and two satellite peaks. $Co2p_{3/2}$ main peak at 781.10 eV, $Co2p_{3/2}$ satellite peak at 786.46 eV, $Co2p_{1/2}$ main peak at 796.09 eV, and $Co2p_{1/2}$ satellite peak at 801.59 eV were identified. This element accounts for 0.36% of the total ZMDBS composition. The high-resolution spectra of Mn2p (Figure 2G) demonstrated that Mn2p peak exhibited a markedly split spin-orbit component (Δ_{metal} = 11.20 eV), manifesting as double peaks with binding energies of 641.79 and 652.99 eV, respectively. This element constituted 0.28% of the total ZMDBS composition.

Those results validated the presence of Mn^{2+}, Mn^{4+} and Co^{2+} in ZMDBS, paving the way for subsequent verification of the ability of ZMDBS to produce reactive oxygen species and generate ·OH, as well as the subsequent assessment of its cellular and animal efficacy. The stability of ZMDBS in water, PBS, RPMI-1640, and DMEM was monitored over a seven-day period (Figure S3). It showed that ZMDBS did not experience substantial precipitation in any of the four solutions after seven days, suggesting exceptional stability of ZMDBS.

The Analysis of the Tumor Microenvironment Responsiveness and CDT Activity

Experiments were performed to determine whether the ZM nanoparticles can interact with excessive GSH in the tumor microenvironment (TME) and address the issue of elevated GSH levels. As shown in Figure 3A, the ZM nanoparticles had a large broad peak at 250–450 nm, which was the characteristic UV–visible absorption peak of MnO_2 nanoparticles. Addition of GSH progressively reduced peak intensity, confirming MnO_2 reduction by GSH and ZM's capacity to deplete excess GSH in the TME. Furthermore, 5, 5'-dithiobis (2-nitrobenzoic acid) (DTNB) was employed as a probe to evaluate the GSH-consuming properties of the nanomaterials.[30] As illustrated in Figure 3B, 100 μM DTNB was incubated with varying concentrations of GSH for a period of 30 min, resulting in the formation of TNB. This product exhibited a distinct UV absorption peak at 412 nm, with the absorbance at this wavelength increasing in proportion to GSH concentration. As illustrated in Figure 3C, a linear regression equation for the absorbance of the TNB product with GSH concentration was derived in a specific concentration range ($y = 0.00598x + 0.03152$; $R^2 = 0.99987$). Subsequently, varying concentrations of ZM were reacted with GSH and DTNB (Figure 3D). Those data provide additional evidence that ZM nanoparticles could consume GSH and demonstrate GSH responsiveness.

In next step, we verified that ZM and ZMDBS could catalyze excess H_2O_2 in the TME to produce ·OH and exert CDT effects. 3, 3', 5, 5'-Tetramethylbenzidine (TMB) was first used as a probe to detect H_2O_2 responsiveness and ROS generation. As shown in Figure 3E, the mixture of TMB and H_2O_2 before the addition of ZM did not show obvious characteristic absorption peaks in the range of 350–750 nm, whereas the solution started to show obvious characteristic absorption peaks at 370 nm and 652 nm after the addition of ZM. The characteristic peaks at 370 and 652 nm gradually

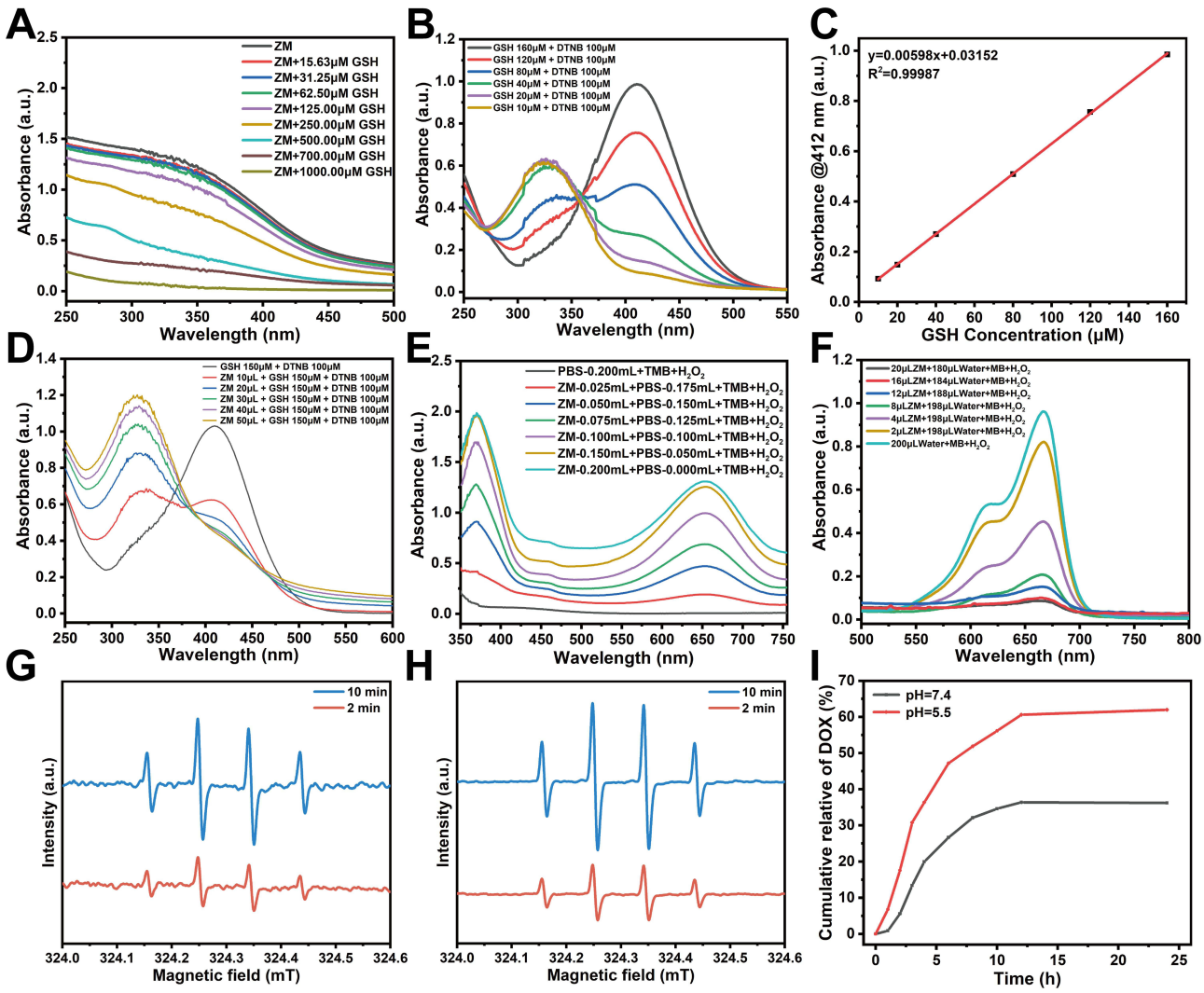

Figure 3 (**A**) UV–visible absorption spectra of the reaction between ZM and different concentrations of GSH; (**B**) UV–visible absorption spectra of the products obtained from the reaction of DTNB with different concentrations of GSH; (**C**) The UV standard curve of the product at 412 nm after the reaction of DTNB with different concentrations of GSH; (**D**) UV–visible absorption spectra of different concentrations of ZM reacting with GSH and DTNB; (**E**) UV–visible absorption spectra of solutions with different concentrations of ZM reacting with H_2O_2 and TMB; (**F**) UV–visible absorption spectra of solutions with different concentrations of ZM reacting with H_2O_2 and MB; (**G**) ESR diagrams of ZM reacting with H_2O_2 at different time points; (**H**) ESR diagrams of ZMDBS reacting with H_2O_2 at different time points; (**I**) Accumulated DOX release curves of ZMDBS at different pH and time points (mean ± SD, n = 3).

increased with increasing ZM concentration, indicating that ZM reacted with H_2O_2 to generate ROS, which gradually increased with the concentration of ZM. Then, methylene blue (MB) was used as a probe to determine the · OH-generating capacity of ZM. MB had a characteristic absorption peak at 665 nm and did not react with H_2O_2. As illustrated in Figure 3F, following the incubation of MB with H_2O_2 for one hour, a pronounced UV absorption peak was observed at 665 nm. The addition of varying concentrations of ZM to the solution resulted in a decrease in the absorption peak at 665 nm, indicating that the reaction of ZM with H_2O_2 resulted in the generation of ·OH, and more ·OH was generated with an increase in ZM concentration. To further verify the ·OH generation ability of the nanomaterials, DMPO was used as the trapping agent and H_2O_2 as the reaction substrate. The types of ROS generated in the reaction system were characterized by adding ZM and ZMDBS at different times. The ESR plots (Figure 3G and 3H) demonstrated that both the ZM and ZMDBS reaction systems produced a 1:2:2:1 signal. Furthermore, the signal at 10 min was stronger than that at 2 min, indicating that both ZM and ZMDBS catalyzed the reaction of H_2O_2 to produce ·OH with CDT activity.

https://doi.org/10.2147/IJN.S546671

To ascertain the efficacy of ZMDBS in releasing DOX under weakly acidic TME conditions, drug release experiments were conducted to assess its drug release capacity under varying pH conditions. As illustrated in Figure 3I, the cumulative release rate of ZMDBS gradually increased with extension of the incubation period, reaching a plateau at approximately 24 h. After 24 h of incubation in a pH=7.4 buffer solution, the cumulative release rate of ZMDBS reached 29.37%. In contrast, the rate was 51.19% when incubated in a pH=5.5 buffer solution for 24 h. These results demonstrated that ZMDBS exhibits pH responsiveness.

In vitro Cellular Uptake, Anti-Tumor Activity, and Biosafety Evaluation of ZMDBS

Effective cellular uptake is essential for drug efficacy. After ZMDBS reacts with H^+ and GSH in the TME, the framework would disintegrate and DOX is released. DOX fluorescence is shown in red, and the nuclei of 4T1 cells fluoresce is blue after staining with DAPI. The intensity of red fluorescence detected via laser confocal microscopy and nuclear localization using DAPI facilitated the assessment of ZMDBS cellular uptake. When ZMDBS was incubated with 4T1 cells for 3 h, 6 h, and 9 h, the nuclei showed strong red fluorescence, indicating that ZMDBS entered the interior of the cells (Figure 4A). To quantify the cellular uptake of DOX at different times of ZMDBS incubation, fluorescence-activated cell sorting (FACS) quantification was performed. FACS quantification showed DOX mean fluorescence intensity increasing over time: 97.73 (0 h), 1429.67 (3 h), 1964.00 (6 h), and 2175.67 (9 h), confirming time-dependent

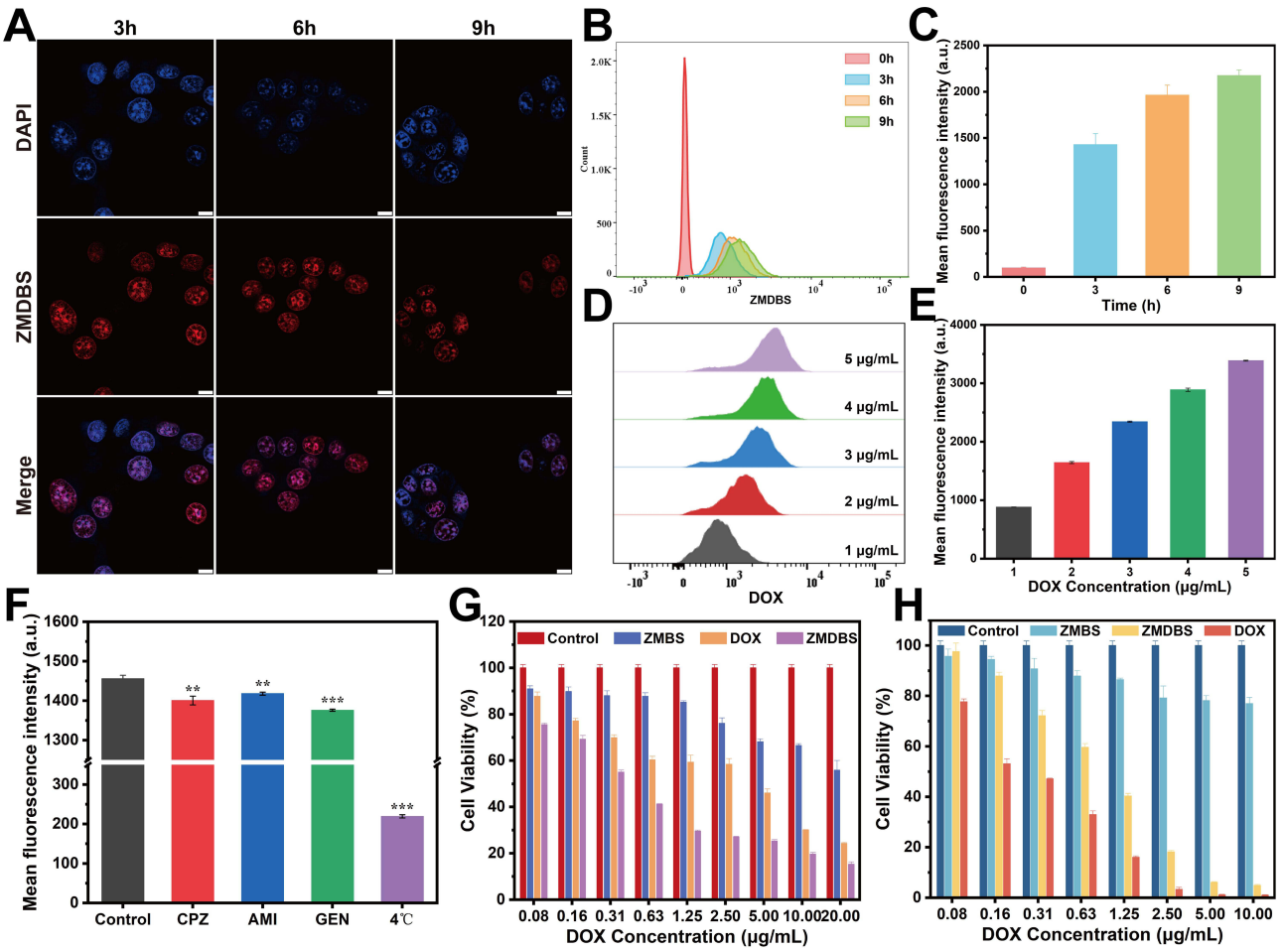

Figure 4 (**A**) CLSM images of ZMDBS co-incubated with 4T1 cells for 3, 6, and 9 h (scale bar = 10 μm); (**B**) FACS plots of ZMDBS co-incubated with 4T1 cells for 3, 6, and 9 h; (**C**) Quantitative histogram of the average fluorescence intensity of ZMDBS incubated with 4T1 cells for 3, 6, and 9 h; (**D**) FACS plots of different concentrations of ZMDBS (in terms of DOX concentration) co-incubated with 4T1 cells; (**E**) Quantitative histogram of the mean fluorescence intensity of different concentrations of ZMDBS (in terms of DOX concentration) incubated with 4T1 cells; (**F**) Quantitative histogram of the mean fluorescence intensity of ZMDBS uptake by 4T1 cells with different inhibitors; (**G**) MTT plots of ZMDBS on 4T1 cells; (**H**) MTT plots of ZMDBS on LO2 cells (mean ± SD, n = 3, $^{**}p<0.01$, $^{***}p<0.001$).

uptake (Figure 4B and 4C). In order to quantitatively analyze the cellular uptake of ZMDBS at different concentrations, varying concentrations of the nanoparticles (1, 2, 3, 4, and 5 μg/mL) were evaluated, and the average fluorescence intensity were 886.00 ± 2.00, 1646.33 ± 18.01, 2344.67 ± 10.02, 2889.67 ± 28.10 and 3386.33 ± 7.02, respectively, demonstrating concentration-dependent uptake (Figure 4D and 4E).

Endocytosis mechanisms were probed using inhibitors chlorpromazine hydrochloride (CPZ), amiloride hydrochloride (AMI), and genistein (GEN); the effect of temperature (4°C) was evaluated as well. The average fluorescence intensity of DOX in Control, CPZ, AMI, GEN and 4°C groups were 1456.00 ± 8.54, 1400.67 ± 11.02, 1418.00 ± 4.00, 1376.00 ± 2.65, 219.33 ± 4.04, respectively (Figure 4F). Among them, 4°C exerted the inhibition suggesting primary energy-dependent endocytosis (fluorescence intensity was 15% versus control). GEN, an inhibitor of caveolin, was involved in the caveolin pathway mediated by the cell membrane. CPZ and AMI also affected the uptake of ZMDBS, suggesting the participation of lattice protein-mediated endocytosis and megaloblast drinking pathways to some extent. In summary, the endocytosis mechanism of ZMDBS was primarily energy-dependent and involved co-assistance from the cytosolic cellar-mediated endocytosis, lattice protein-mediated endocytosis, and mega-cellular drinking pathways.

Live and dead 4T1 cells staining via fluorescence microscopy after 24 h treatment revealed fewer live cells in ZMDBS vs control group, followed by DOX group (Calcein-AM staining). PI staining revealed that the ZMDBS group exhibited the highest number of deceased cells compared with the control group, followed by the DOX group (Figure S4). Therefore, both staining assays could be preliminarily inferred that ZMDBS has an effective anti-tumor effect and surpasses that of the single-agent DOX group. Subsequently, the cytotoxicity of ZMDBS to 4T1 cells was evaluated by MTT assay. The concentrations of ZMBS, ZMDBS were normalized to the DOX concentration. As illustrated in Figure 4G, ZMBS modestly reduced 4T1 cell viability relative to the control, likely due to its TNBC-responsive release of Co^{2+} and Mn^{2+} at the tumor site, which catalyze intracellular H_2O_2 to •OH (via Fenton-like reaction) and induced cytotoxicity. Both DOX and ZMDBS exhibited dose-dependent anti-tumor effects, with calculated IC_{50} values of 5.00 ± 0.91 μg/mL for DOX and 0.35 ± 0.06 μg/mL for ZMDBS, indicating markedly greater potency of ZMDBS versus single-agent DOX.

The biosafety profile was evaluated in LO2 cells (Figure 4H). Cytotoxicity of DOX and ZMDBS increased with dose, whereas the ZMBS carrier showed comparatively lower toxicity at higher concentrations. At a DOX dose of 10 μg/mL (equivalent to 77.72 μg/mL ZMBS and 87.72 μg/mL ZMDBS according to the molar ratio), LO2 cell survival was 77.00 ± 2.48% for ZMBS, 0.97 ± 0.26% for DOX, and 4.90 ± 0.39% for ZMDBS, suggesting that BSA within the carrier mitigates nanomaterial toxicity and that DOX loading in ZMDBS partially reduced DOX-induced cytotoxicity. Overall, ZMDB/ZMDBS demonstrated improved in vitro safety compared with single-agent DOX, supporting subsequent in vivo evaluation. In vitro hemolysis assays further confirmed ZMDBS safety, with saline and deionized water as negative and positive controls, respectively (Figure S5). Exposure of erythrocytes to ZMDBS in saline at varying concentrations induced <5% hemolysis, even at the highest dose, underscoring its favorable biocompatibility under physiological conditions.

ZMDBS-Induced ROS Generation and Cell Apoptosis

The Nano-delivery system ZMDBS penetrates tumor cells and reacts with GSH and H^+ to generate Co^{2+} and Mn^{2+}, which catalyze Fenton reactions converting excess H_2O_2 to produce ·OH. Simultaneously, DOX activates NADPH oxidase under normoxic conditions to generate $\cdot O_2^-$ from O_2, which can be further transformed to H_2O_2 by superoxide dismutase (SOD) and enhances CDT efficacy. The anti-tumor effects of ZMDBS are primarily attributed to ROS generation. Therefore, it was essential to verify the ability of ZMDBS to produce ROS.

As shown in Figure 5A, ZMBS, DOX, and ZMDBS groups exhibited strong green fluorescence versus the control, confirming ROS production by ZMBS and ZMDBS; ZMDBS showed enhanced fluorescence over ZMBS, indicating chemotherapy-CDT synergy. Subsequently, the ability of ZMDBS to stimulate ROS generation in 4T1 cells was assessed using flow cytometry. The mean DCF fluorescence intensities were: 815.33 ± 49.12 (control), 1514.67 ± 184.07 (ZMBS), 2043.67 ± 122.70 (DOX), and 2732.00 ± 108.06 (ZMDBS) (Figures 5B and 5C). Those data showed ZMDBS generated significantly more ROS than DOX or ZMBS, demonstrating its superior induction of ROS for the combined treatment with chemotherapy and CDT.

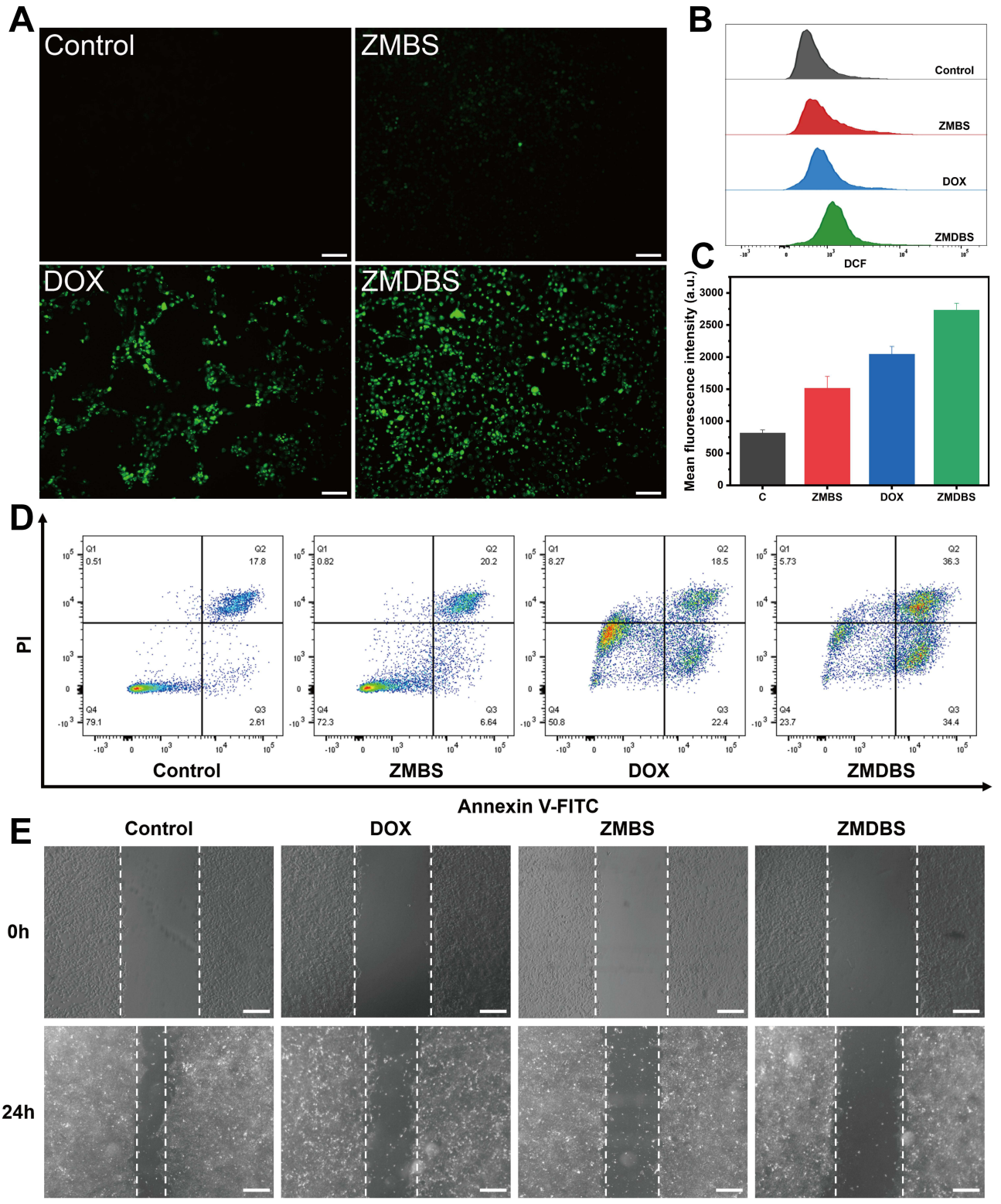

Figure 5 (**A**) Inverted fluorescent map of ZMDBS reactive oxygen species experiments (scale bar = 100 μm); (**B**) FACS plots of ROS generated by different groups; (**C**) Quantitative histogram of relative fluorescence intensity of ROS produced by different groups (mean ± SD, n = 3); (**D**) Quantitative FACS plots of different groups inducing apoptosis in 4T1 cells; (**E**) Inverted fluorescence maps of cell scratches after 0 h and 24 h of treatment of 4T1 cells with different materials (scale bar = 300 μm).

The effect of ZMDBS on the induction of apoptosis in 4T1 cells was investigated using an Annexin V-FITC/PI apoptosis detection kit. As shown in Figure 5D, the percentage of total apoptosis (early and late apoptosis) in the ZMDBS group was 70.7 ± 0.85%, which was higher than that in the DOX (40.9 ± 0.36%) and ZMBS (26.84 ± 0.33%) groups, confirming its enhanced apoptotic efficacy. Cell migration inhibition was assessed via scratch assay (Figure 5E). After 24 h of incubation in a serum-free culture medium, the control group exhibited robust cell migration. In contrast, cell migration was significantly suppressed in the DOX and ZMBS groups, with the most pronounced inhibition observed in the ZMDBS group. The mechanism probably accounts from the poisoning of topoisomerase II by DOX, and the enhance CDT and ROS generation by ZMBS, which suggested that ZMDBS has a notable inhibitory effect on cell migration.

Transcriptomic Analysis of ZMDBS

Transcriptomic sequencing analyzed 4T1 cells treated with PBS (control group) or ZMDBS to elucidate its anti-tumor mechanism. The volcano plot (Figure 6A) showed 11,502 differentially expressed genes (DEGs) between ZMDBS and control groups, with 7,017 upregulated and 4,485 downregulated. GO enrichment analysis (Figure 6B) identified the top 30 terms, revealing ZMDBS impacts proteasomal proteolytic processes, mitotic cell cycle regulation, post-transcriptional gene expression, and intrinsic apoptotic signaling pathways. KEGG enrichment (Figure 6C) highlighted 20 key pathways, including miRNA activation in cancer, cell cycle, viral carcinogenesis, and aminoacyl-tRNA biosynthesis.

Previous studies have confirmed ZMDBS's anti-TNBC effects via ROS generation, inhibition of 4T1 cell proliferation/migration, and apoptosis induction. GO/KEGG results further indicated influences on cell cycle, proliferation, invasion, migration, apoptosis, and intracellular signaling in 4T1 cells. It has been observed that an excess of ROS disrupts the balance between oxidative and antioxidant capacities within cancer cells and triggers enhanced apoptosis when critical thresholds are surpassed.[31] Therefore, to explore ROS-induced apoptosis, we focused on enriched pathways: p53,[32] MAPK,[33] and TNF,[34] for further analysis.

In the p53 pathway (Figure 6D), 62 DEGs were enriched in ZMDBS vs control (39 upregulated, 23 downregulated). Per the mechanism diagram (Figure S6), ZMDBS activates p53, upregulating p21, Gadd45, IGF-BP3, BAI-1, and p53 R2, while downregulating Cyclin D, CDK4/6, and Bcl2, causing G1/G2 arrest and activating CASP9/CASP3 for apoptosis. The MAPK pathway (Figure 6E) had 185 DEGs (101 upregulated, 84 downregulated). Mechanism diagram (Figure S7) showed upregulation of CACN, GF, TNF, RTK, HSP72, PTP, and MKP, and downregulation of IL1, TGFBR, Ras, AKT, and p38, indirectly activating p53, Wnt, and apoptosis pathways. The TNF pathway (Figure 6F) exhibited 83 DEGs (54 upregulated, 29 downregulated). Mechanism (Figure S8) indicated ZMDBS activates TNF, then TNFR1/TNFR2, upregulating TRADD, TRAF series, RIP3, CASP8/10, CREB, and cIAP1/2, while downregulating Akt and p38, impacting DNA activation and adjacent apoptosis. For the apoptosis pathway (Figure 6G, mechanism in Figure 6H), 92 DEGs were enriched (46 upregulated, 46 downregulated). ZMDBS activates TNFα and TRAIL, then TRAIL-R and TNF-R1, modulating ASK1, CHOP, CASP8, IP3R, and NF-κB, culminating in apoptosis.

In summary, transcriptomic analysis showed ZMDBS induces ROS overproduction in 4T1 cells, activating p53, MAPK, and TNF pathways, which triggers cascades leading to apoptosis pathway activation and cell death.

In vivo Imaging of ZMDBS Distribution Using ICG-Loaded ZMBS

Indocyanine green (ICG), a near-infrared imaging agent approved by the FDA for clinical application, exhibits a distinct near-infrared (NIR) characteristic absorption peak and is widely used for in vivo imaging. DOX's excitation (480 nm) and emission (560 nm) wavelengths offer poor tissue penetration, are hindered by animal autofluorescence, and suffer from self-quenching, making it unsuitable for in vivo probes. Therefore, in this study, ICG was adopted to replace DOX and encapsulated in ZMBS to simulate ZMDBS tissue distribution in mice post-administration.

The results (Figure 7A and 7B) indicated that after tail vein injection, fluorescence intensity of ICG-ZMBS and free ICG at the tumor site peaked at 3 h and gradually declined. This suggests that ICG-ZMBS was gradually metabolized by the body which referred to the clinical application of ICG.[35,36] The higher fluorescence intensity at the tumor site in the ICG-ZMBS group than in the ICG group may be attributed to ZMBS encapsulation, which made ICG-ZMBS responsive to the tumor microenvironment and more likely to accumulate at the tumor site. Additionally, fluorescence imaging maps

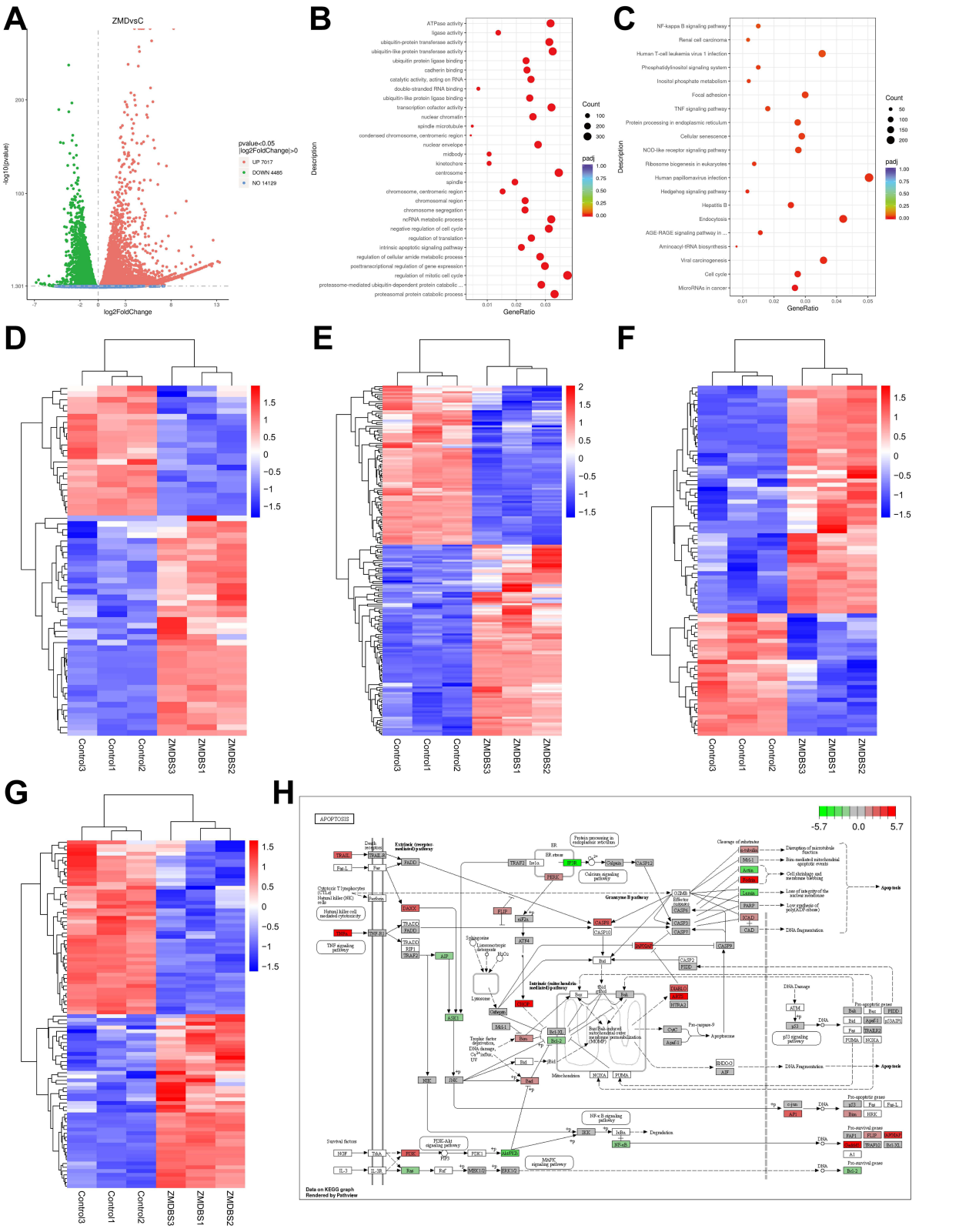

Figure 6 ZMDBS group compared with control group of (**A**) volcano plot of differential gene expression; (**B**) bubble plot of GO enrichment analysis; (**C**) bubble plot of KEGG enrichment analysis; (**D**) clustering heatmap of differentially expressed genes in p53 pathway; (**E**) clustering heatmap of differentially expressed genes in MAPK pathway; (**F**) clustering heatmap of differentially expressed genes in TNF pathway; (**G**) clustering heatmap of differentially expressed genes in apoptosis pathway; (**H**) apoptosis pathview graph.

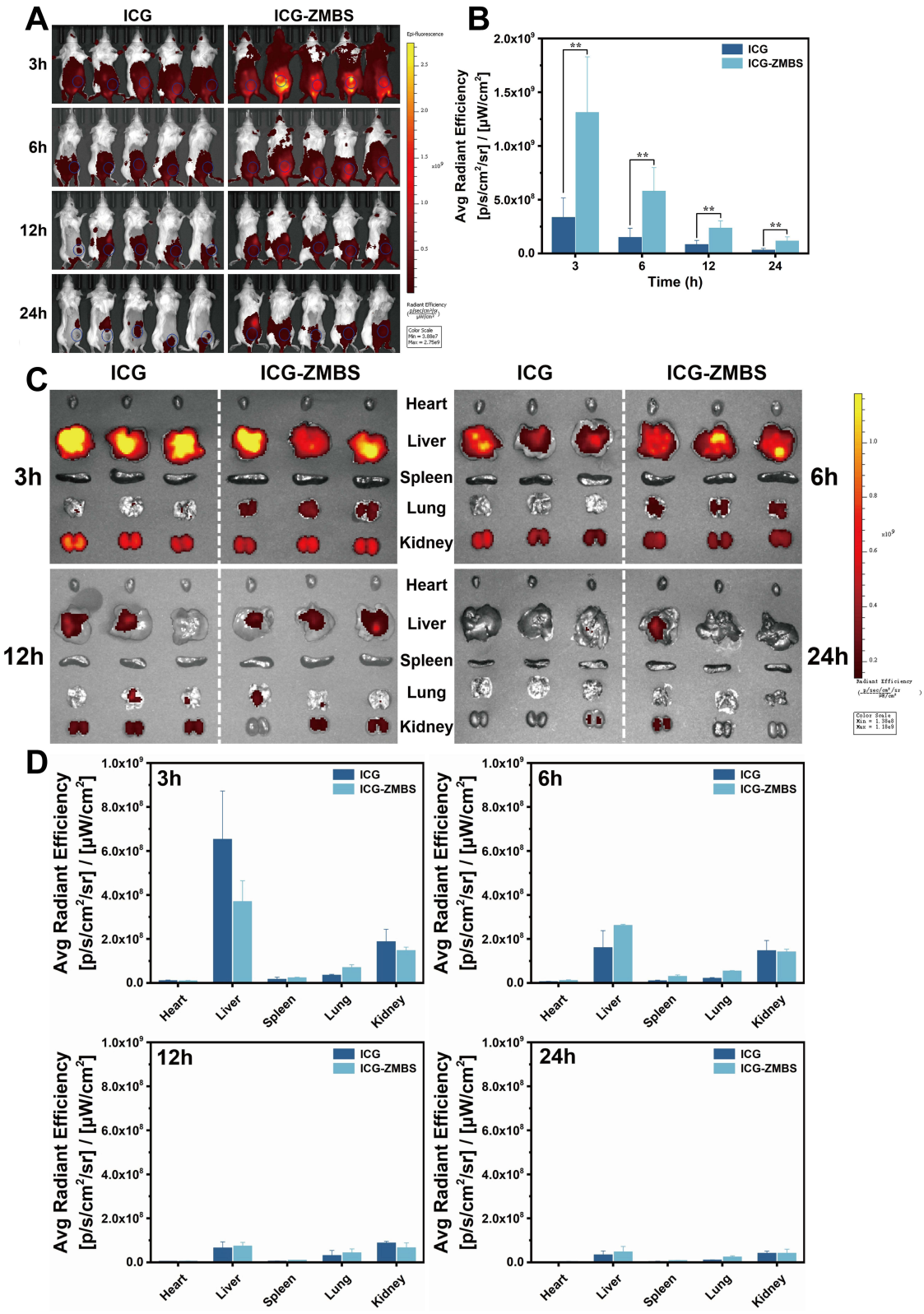

Figure 7 (**A**) Fluorescence imaging maps of ICG and ICG-ZMBS distribution in mice at different time points; (**B**) Quantitative histograms of ICG and ICG-ZMBS fluorescence at tumor sites in living mice at different time points (mean ± SD, n = 5, $^{**}p < 0.01$); (**C**) Fluorescence imaging maps of isolated organs in mice at different time points; (**D**) Quantitative fluorescence intensity plots of isolated mouse organs at 3 h, 6 h, 12 h and 24 h (mean ± SD, n = 3).

https://doi.org/10.2147/IJN.S546671

of isolated organs (Figure 7C and 7D) showed that liver and kidney the exhibited the highest fluorescence in both groups, followed by lungs, with minimal in heart and spleen. Organ fluorescence peaked at 3 h and decreased over time, aligning with in vivo tissue distribution results. These findings showed that the majority of drugs were metabolized within 24 h, indicating favorable in vivo biosafety. Furthermore, ICG-ZMBS fluorescence in liver and kidney was higher than free ICG after 3 h, implying improved circulation and reduced rapid clearance. All of the results underscored the excellent tumor microenvironment responsiveness, biocompatibility, and biological safety of ZMBS.

In vivo Therapeutic Efficacy of ZMDBS in 4T1 Tumor-Bearing Mice

Due to the potent anti-tumor effect of ZMDBS observed in vitro, its in vivo efficacy was evaluated in 4T1 tumor-bearing mice. As depicted in Figure 8A, the control group (administered with saline) exhibited rapid tumor growth, reaching the average tumor volume of 708.90 ± 121.19 mm^3 by day 12. The ZMBS group (561.65 ± 92.85 mm^3) and DOX group (488.25 ± 68.98 mm^3) showed moderate inhibition. The tumor growth curve of the DOX group was smoother than that of the control and ZMBS groups, owing to the chemotherapeutic effect of DOX. In comparison to these three groups, ZMDBS exhibited the slowest growth (278.77 ± 17.72 mm^3), signifying a superior inhibition effect on tumor growth compared to single-agent DOX. After measuring the tumor size and body weight of the mice in each group on the 12th day, the mice were euthanized, images of the tumors were taken, and their weights were recorded (Figure 8B and 8C).

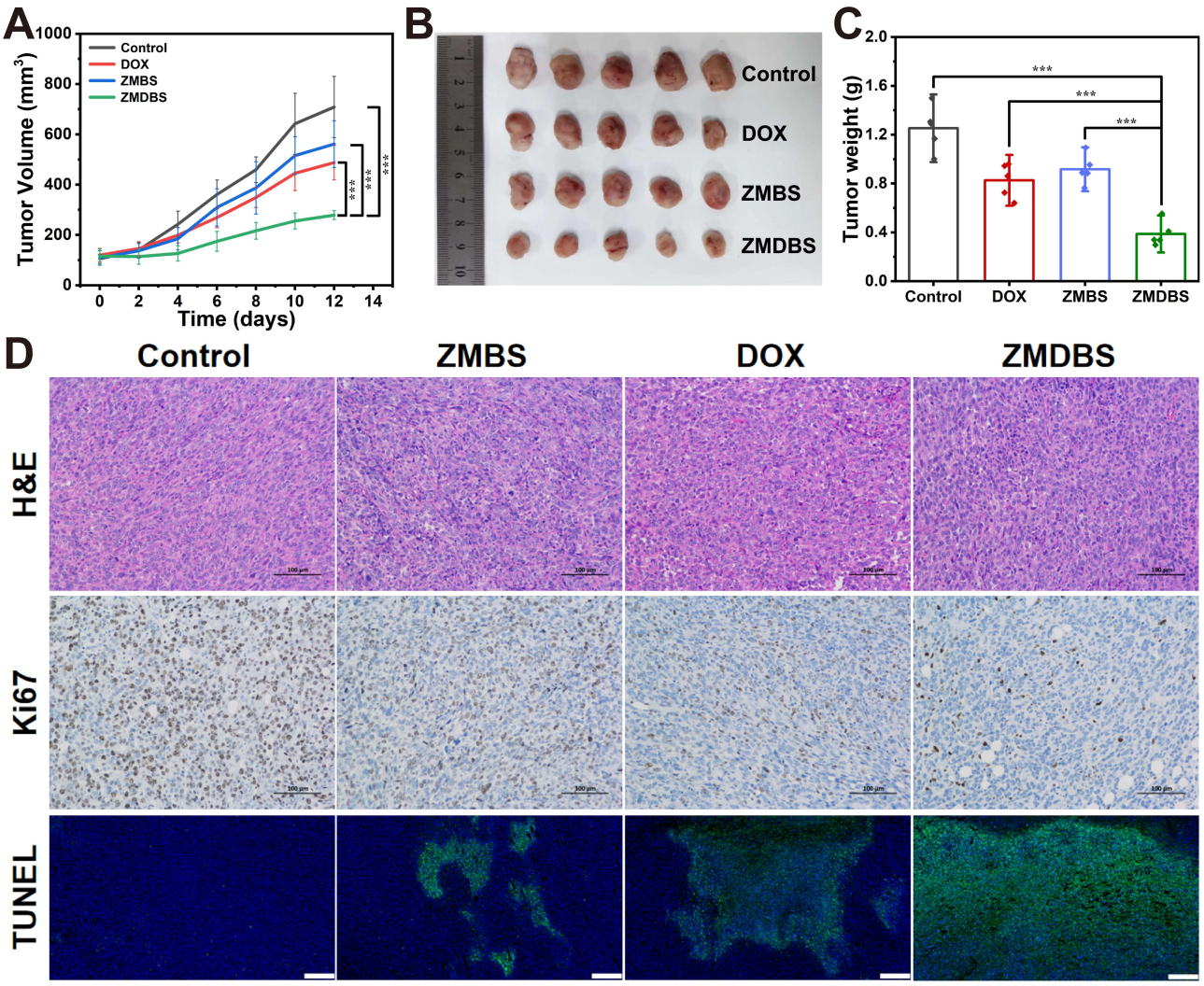

Figure 8 Different groups of (**A**) tumor growth curve; (**B**) in vitro tumor images; (**C**) in vitro tumor weight; (**D**) H&E, Ki67, and TUNEL staining results (mean ± SD, n = 5, ***p<0.001). Note: the scale for TUNEL images is 300μm.

The results indicated that the control group exhibited the largest isolated tumor size and weight values, followed by the ZMBS and DOX groups, whereas the ZMDBS group was the smallest. Based on the ZMDBS in vivo tissue distribution experiment, this outcome may be attributed to ZMDBS's responsiveness to the TME, allowing it to preferentially accumulate at the tumor site and harness the advantages of chemotherapy and CDT combination therapy to further inhibit tumor growth. Additionally, mouse body weights were observed stable over 12 consecutive days post-administration (Figure S9), indicating that the adverse reactions to ZMDBS in vivo remained within a manageable range.

Mice were euthanized at the conclusion of the treatment, and tumor tissues were prepared for H&E, Ki67, and TUNEL staining (Figure 8D). H&E staining demonstrated that the morphology of tumor cells in the control group was predominantly well-preserved, whereas those in the ZMBS, DOX, and ZMDBS groups exhibited wrinkling, contraction, nuclear solidification, and fragmentation. Ki67 staining indicated high proliferation of tumor cells in control group (a higher proportion of brownish-yellow coloration), and a reduction in tumor cell activity in ZMBS and DOX groups. The ZMBS group exhibited minimal brownish-yellow staining, indicating the lowest levels of tumor cell activity and proliferation. TUNEL staining revealed that the control group had the lowest percentage of apoptotic cells in the tumor tissues (weakest green fluorescence intensity). The ZMBS and DOX groups showed partial green fluorescence, suggesting the presence of partially apoptotic cells in their respective tumor tissues. The prevalence of green fluorescence in the ZMDBS group indicated a significant presence of apoptotic cells in tumor tissues, suggesting that ZMDBS demonstrated superior anti-tumor efficacy compared to ZMBS and DOX. Those findings (H&E, Ki67, and TUNEL staining) were consistent with the results of previous in vitro biological evaluations, further confirming that the inhibitory effects of ZMDBS on tumor growth.

Additionally, H&E staining of the major organs showed no damage or inflammation (Figure S10), indicating the favorable histocompatibility and biosafety of ZMDBS. The assessment of biochemistry markers: alanine aminotransferase (ALT), aspartate aminotransferase (AST), total bilirubin (TBIL), direct bilirubin (DBIL), serum albumin (ALB), alkaline phosphatase (ALP), γ-glutamyltransferase, urea nitrogen (BUN), and creatinine (CREA), were all within the normal reference ranges for mice (Figure S11), confirming the safe dosage and ZMDBS's favorable biosafety.

In summary, the nano-delivery system ZMDBS demonstrated significant tumor growth inhibition while exhibiting favorable biocompatibility in vivo, offering potential for the clinical treatment of TNBC.

Conclusion

In this study, we successfully developed a novel pH/H_2O_2 dual-responsive cobalt/manganese-based nano-delivery system called ZMDBS. The anti-tumor efficacy and TME responsiveness of ZMDBS were demonstrated through comprehensive in vitro and in vivo biological evaluation. Unlike the traditional MnO_2-based CDT agents, which effectively deplete GSH and generate ·OH, but often suffer from limited tumor accumulation and high off-target toxicity due to non-specific release.[37–39] By introducing ZIF-67, BSA, and SDS, ZMDBS had better TME-specific targeting and DOX co-delivery, achieving a nearly 14-fold lower IC_{50} (0.35 μg/mL vs 5.00 μg/mL for free DOX) and superior in vivo tumor inhibition (78% volume reduction vs 31% for single-agent DOX). Moreover, compared to dual-responsive systems like Cu-MOF/GOx hybrids, which enhance H_2O_2 supply but exhibit potential Cu-induced cytotoxicity.[40,41] ZMDBS demonstrated better biocompatibility (eg, <5% hemolysis, normal organ function markers) and adaptability to TNBC's acidic TME without exogenous enzyme addition. These characteristics, combined with the synergistic effect of CDT chemotherapy, make ZMDBS a more efficient and safer platform, which is confirmed by its longer circulation time and lower liver/kidney clearance rate compared with non-albuminized counterparts.

Although the transcriptomic analysis revealed that the induction of ROS overproduction by ZMDBS was through p53, MAPK, and TNF pathways, future research should involve validating the pharmacological mechanism of ZMDBS using molecular biology experiments (eg, Western blot) or gene knockout animal models based on transcriptomic data. To enrich the preclinical safety and pharmacodynamics research, a long-term toxicity experiment (30-day) or the assessment of other TNBC models (eg, MDA-MB-231) could be planned for next step. Moreover, the common reagents used for the synthesis of ZMDBS make it possible for an industrial production. Further optimization of the scale-up synthesis process and a comprehensive stability assessment (eg batch consistency) should ensure its feasibility for clinical application. Overall, those studies will promote ZMDBS's clinical translation and application.

Acknowledgments

This research was supported by the Natural Science Foundation of Fujian Province, China (No. 2023J01311), the High Level Talent Foundation of Fujian Medical University (No. XRCZX2021005), the Young Teachers Education Foundation of Fujian Province, China (No. JAT220080), Joint Funds at the Innovation of Science and Technology, Fujian Province, China (No. 2021Y9008), Natural Science Foundation of China (No. 22074017), and Key Project Supported by the Natural Science Foundation of Fujian Province, China (No. 2021J02034).

Author Contributions

All authors made a significant contribution to the work reported, whether that is in the conception, study design, execution, acquisition of data, analysis and interpretation, or in all these areas; took part in drafting, revising or critically reviewing the article; gave final approval of the version to be published; have agreed on the journal to which the article has been submitted; and agree to be accountable for all aspects of the work.

Disclosure

The authors report no conflicts of interest in this work.

References

1. Leon-Ferre RA, Goetz MP. Advances in systemic therapies for triple negative breast cancer. *BMJ*. 2023;381:e071674. doi:10.1136/bmj-2022-071674
2. Choupani E, Gomari MM, Zanganeh S, et al. Newly developed targeted therapies against the androgen receptor in triple-negative breast cancer: a review. *Pharmacol Rev*. 2023;75(2):309–327. doi:10.1124/pharmrev.122.000665
3. He F, Xie C, Xu X. Hyaluronic acid-modified yeast β-glucan particles delivering doxorubicin for treatment of breast cancer. *Carbohydr. Polym*. 2023;314:120907. doi:10.1016/j.carbpol.2023.120907
4. Lim C, Hwang D, Yazdimamaghani M, et al. High-dose paclitaxel and its combination with CSF1R inhibitor in polymeric micelles for chemoimmunotherapy of triple negative breast cancer. *Nano Today*. 2023;51:101884. doi:10.1016/j.nantod.2023.101884
5. Hao D, Meng Q, Li C, et al. A paclitaxel prodrug with copper depletion for combined therapy toward triple-negative breast cancer. *ACS Nano*. 2023;17(13):12383–12393. doi:10.1021/acsnano.3c01792
6. Zhou Z, Ke Q, Wu M, Zhang L, Jiang K. Pore space partition approach of zif-8 for ph responsive codelivery of ursolic acid and 5-fluorouracil. *ACS Mater Lett*. 2023;5(2):466–472. doi:10.1021/acsmaterialslett.2c01097
7. Yao Z, Hu Q, Jin P, et al. A self-assembly combined nano-prodrug to overcome gemcitabine chemo-resistance of pancreatic tumors. *Adv. Funct. Mater*. 2023;33(30):2214598. doi:10.1002/adfm.202214598
8. Hejmady S, Pradhan R, Alexander A, et al. Recent advances in targeted nanomedicine as promising antitumor therapeutics. *Drug Discovery Today*. 2020;25(12):2227–2244. doi:10.1016/j.drudis.2020.09.031
9. Li J, Dai J, Zhao L, et al. Bioactive Bacteria/MOF hybrids can achieve targeted synergistic chemotherapy and chemodynamic therapy against breast tumors. *Adv. Funct. Mater*. 2023;33(42):2303254. doi:10.1002/adfm.202303254
10. Wu J, Meng Y, Wu F, et al. Ultrasound-driven non-metallic fenton-active center construction for extensive chemodynamic therapy. *Adv. Mater*. 2024;36(2):2307980. doi:10.1002/adma.202307980
11. Sun D, Sun X, Zhang X, et al. Emerging chemodynamic nanotherapeutics for cancer treatment. *Adv. Healthcare Mater*. 2024;13(22):e2400809. doi:10.1002/adhm.202400809
12. Zhou Y, Fan S, Feng L, Huang X, Chen X. Manipulating intratumoral fenton chemistry for enhanced chemodynamic and chemodynamic-synergized multimodal therapy. *Adv. Mater*. 2021;33(48):2104223. doi:10.1002/adma.202104223
13. Jiang Y, Lu H, Lei L, Scherman D, Liu Y. Tumor microenvironment-responsive MIL-53 (Fe)@ MnO_2-induced glutathione depletion and sustained hydroxyl radical generation for enhanced chemodynamic cancer therapy. *J Colloid Interface Sci*. 2025;700:138342. doi:10.1016/j.jcis.2025.138342
14. Chen Z, Wang X, Ding Y, Xing C, Lu C, Tu X. A self-assembled copper-selenocysteine nanoparticle for enhanced chemodynamic therapy via oxidative stress amplification. *ACS Mater Lett*. 2023;5(4):1237–1244. doi:10.1021/acsmaterialslett.2c01024
15. Zhong X, Wang X, Cheng L, et al. GSH-Depleted $PtCu_3$ nanocages for chemodynamic- enhanced sonodynamic cancer therapy. *Adv. Funct. Mater*. 2020;30(4):1907954. doi:10.1002/adfm.201907954
16. Xu Z, Zhang L, Gong M, et al. Fe-mediated self-assembled nanodrug for tumor microenvironment activated synergistic ferroptosis-based-chemodynamic/chemo therapy and magnetic resonance imaging. *ACS Mater Lett*. 2024;6(2):656–665. doi:10.1021/acsmaterialslett.3c01265
17. Lim YG, Chang Y, Park S-J, Kim K-D, Park K. Multifunctional and endogenous stimuli-responsive vinblastine sulfate/manganese dioxide nanodrugs for enhancing chemotherapeutic efficacy against hypoxic tumors. *Mater Today Bio*. 2025;34:102229. doi:10.1016/j.mtbio.2025.102229
18. Ushio-Fukai M, Nakamura Y. Reactive oxygen species and angiogenesis: NADPH oxidase as target for cancer therapy. *Cancer Lett*. 2008;266(1):37–52. doi:10.1016/j.canlet.2008.02.044
19. Li J, Li Y, Wang Y, et al. A proton pump inhibitor-programmed ROS generator enhances the synergistic efficacy of chemo-/chemodynamic therapy with reduced renal injury. *Chem Eng J*. 2025;505:159201. doi:10.1016/j.cej.2024.159201
20. Mao L, Lu J, Wen X, et al. Cuproptosis: mechanisms and nanotherapeutic strategies in cancer and beyond. *Chem. Soc. Rev*. 2025. doi:10.1039/D5CS00083A
21. Nejabat M, Samie A, Khojastehnezhad A, et al. Stimuli-responsive covalent organic frameworks for cancer therapy. *ACS Appl. Mater. Interfaces*. 2024;16(39):51837–51859. doi:10.1021/acsami.4c07040

22. Cao X, Feng N, Huang Q, Liu Y. Nanoscale metal–organic frameworks and nanoscale coordination polymers: from synthesis to cancer therapy and biomedical imaging. *ACS Appl. Bio Mater.* 2024;7(12):7965–7986. doi:10.1021/acsabm.3c01300
23. Prasad P, Gordijo CR, Abbasi AZ, et al. Multifunctional Albumin–MnO_2 nanoparticles modulate solid tumor microenvironment by attenuating hypoxia, acidosis, vascular endothelial growth factor and enhance radiation response. *ACS Nano*. 2014;8(4):3202–3212. doi:10.1021/nn405773r
24. Ji C, Xu J, Jiang Q, et al. Significantly boosted photoelectrochemical water splitting performance by plasmonic enhanced Hematite@MOF composite photoelectrodes. *Mater Today Adv.* 2023;18:100361. doi:10.1016/j.mtadv.2023.100361
25. Liu Y, Qin L, Qin Y, et al. Electrocatalytic degradation of nitrogenous heterocycles on confined particle electrodes derived from ZIF-67. *J Hazard Mater.* 2024;463:132899. doi:10.1016/j.jhazmat.2023.132899
26. Liu Z, Sun D, Wang C, et al. Zeolitic imidazolate framework-67 and its derivatives for photocatalytic applications. *Coord. Chem. Rev.* 2024;502:215612. doi:10.1016/j.ccr.2023.215612
27. Villalgordo-Hernández D, Antonio Diaz-Perez M, Balloi V, et al. Post-synthetic ligand exchange as a route to improve the affinity of ZIF-67 towards CO_2. *Chem Eng J*. 2023;476:146846. doi:10.1016/j.cej.2023.146846
28. Wu Q, Gu J, Wang J, Liu N, Chaemchuen S. Impact in rational synthesis Co-ZIF templates for derived the structural Co@NC catalysis for high efficient hydrogen and oxygen evolution reactions. *Int J Hydrogen Energy.* 2023;48(7):2663–2676. doi:10.1016/j.ijhydene.2022.10.120
29. Zhong G, Liu D, Zhang J. The application of ZIF-67 and its derivatives: adsorption, separation, electrochemistry and catalysts. 10.1039/C7TA08268A. *J Mater Chem A*. 2018;6(5):1887–1899. doi:10.1039/C7TA08268A
30. Wen Y, Qiu Q, Feng F, et al. Tailored biomimetic nanoreactor improves glioma chemodynamic treatment via triple glutathione depletion and prompt acidity elevation. *Mater Today Bio*. 2025;30:101447. doi:10.1016/j.mtbio.2025.101447
31. Sanati M, Afshari AR, Kesharwani P, Sukhorukov VN, Sahebkar A. Recent trends in the application of nanoparticles in cancer therapy: the involvement of oxidative stress. *J Control Release*. 2022;348:287–304. doi:10.1016/j.jconrel.2022.05.035
32. Chen J, Yan L, Zhang Y, et al. Maternal exposure to nanopolystyrene induces neurotoxicity in offspring through P53-mediated ferritinophagy and ferroptosis in the rat hippocampus. *J Nanobiotechnol*. 2024;22(1):651. doi:10.1186/s12951-024-02911-9
33. Fang S, Sun S, Cai H, et al. IRGM/Irgm1 facilitates macrophage apoptosis through ROS generation and MAPK signal transduction: irgm1 ± mice display increases atherosclerotic plaque stabilityResearch Paper. *Theranostics*. 2021;11(19):9358–9375. doi:10.7150/thno.62797
34. Shi X, Xu T, Li X, et al. ROS mediated pyroptosis-M1 polarization crosstalk participates in inflammation of chicken liver induced by bisphenol A and selenium deficiency. *Environ. Pollut*. 2023;324:121392. doi:10.1016/j.envpol.2023.121392
35. Esposito C, Del Conte F, Cerulo M, et al. Clinical application and technical standardization of indocyanine green (ICG) fluorescence imaging in pediatric minimally invasive surgery. *"Pediatr. Surg. Int*. 2019;35(10):1043–1050. doi:10.1007/s00383-019-04519-9
36. Reinhart MB, Huntington CR, Blair LJ, Heniford BT, Augenstein VA. Indocyanine green: historical context, current applications, and future considerations. *Surgical Innovation*. 2016;23(2):166–175. doi:10.1177/1553350615604053
37. Liu Y, Pan Y, Cao W, et al. A tumor microenvironment responsive biodegradable $CaCO_3$/MnO_2-based nanoplatform for the enhanced photodynamic therapy and improved PD-L1 immunotherapy. *Theranostics*. 2019;9(23):6867. doi:10.7150/thno.37586
38. Wu M, Liao Y, Guo D, et al. Manganese-based nanomaterials in diagnostics and chemodynamic therapy of cancers: new development. *RSC Adv.* 2024;14(21):14722–14741. doi:10.1039/D4RA01655F
39. Zhang K, Qi C, Cai K. Manganese-based tumor immunotherapy. *Adv. Mater.* 2023;35(19):2205409. doi:10.1002/adma.202205409
40. Chen C, Wang Y-L, Lin X, Ma S-H, Cao J-T, Liu Y-M. Cu-MOFs/GOx bifunctional probe-based synergistic signal amplification strategy: toward highly sensitive closed bipolar electrochemiluminescence immunoassay. *ACS Appl. Mater. Interfaces*. 2023;15(19):22959–22966. doi:10.1021/acsami.3c02381
41. Aggarwal V, Solanki S, Malhotra BD. Applications of metal–organic framework-based bioelectrodes. *Chem. Sci*. 2022;13(30):8727–8743. doi:10.1039/D2SC03441G